Lecture 5:
Tokamak Discharge Control

AP 4990y Seminar
Columbia University
Spring, 2011

Control Topics:

- Wall conditioning
- Plasma operation scenario sequencing
- Plasma basic control (magnetic and kinetic)
- Plasma advanced control (control of RWMs, NTMs, ELMs, error fields, etc), and
- Plasma fast shutdown

References

- ITER. Chapter 8: Plasma operation and control. Nuclear Fusion (1999) vol. **39** (12) pp. 2577. (Original, double-sized ITER.)
- Hawryluk. et al, "Principal physics developments evaluated in the ITER design review." Nucl. Fusion (2009) vol. **49** (065012) pp. 065012
- ★ Gribov et al. "Chapter 8: Plasma operation and control," Nucl Fusion (2007) vol. **47** (6) pp. S385-S403. (Only "**basic plasma control**".)
- Sips et al. "Experimental studies of ITER demonstration discharges," Nuclear Fusion (2009) vol. **49** pp. 085015
- Kessel et al. "Development of ITER 15 MA ELMy H-mode inductive scenario." Nuclear Fusion (2009) vol. **49** pp. 085034.
- ➡ Jardin et al. "Dynamic modeling of transport and positional control of tokamaks." Journal of Computational Physics (1986) vol. **66** (2) pp. 481-507

Wall Conditioning

- Bake components and vessel (water/HCs)
- Once a month: glow (when TF off)
- TF "on" for weeks at a time: ICRH & ECR discharge cleaning (with no PF cycling.)
- T retention/removal (?)

Control data access and communication (CODAC) system and in some types of off-normal operations by the central interlock system (CIS) and central safety systems (CSS)

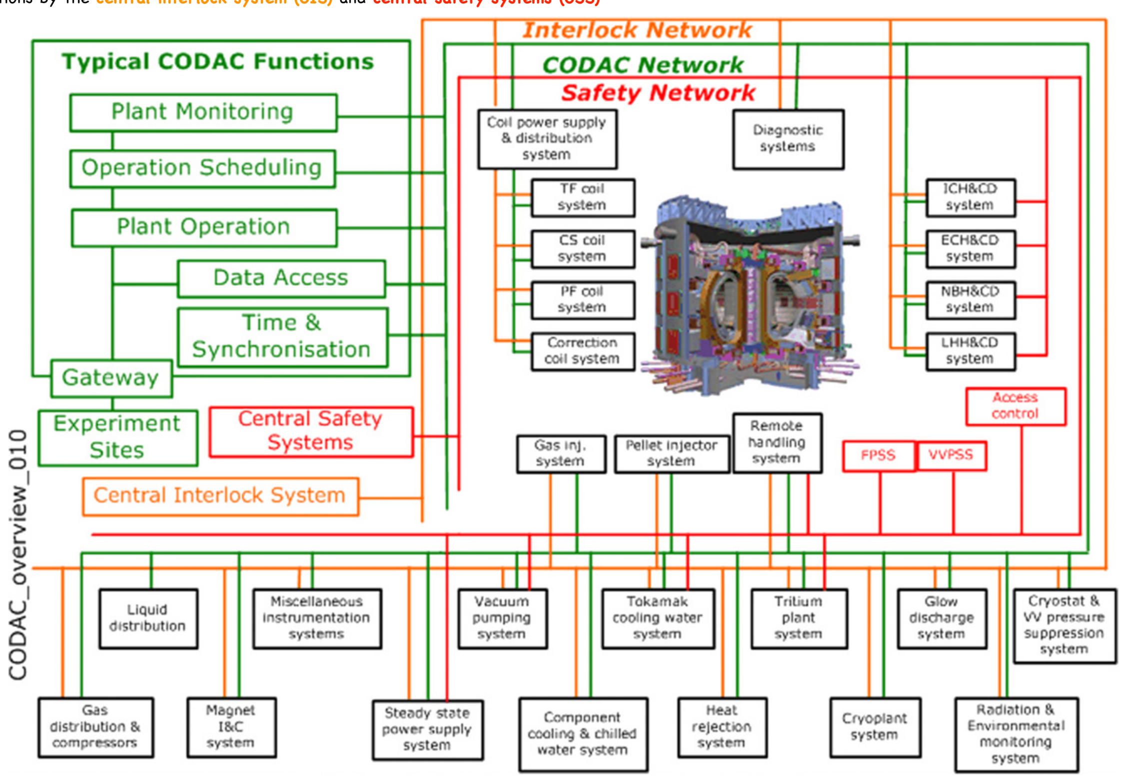

Figure 1. Simplified scheme of the ITER plant control system.

Plasma Control

- Plasma initiation (breakdown, ramp-up, start-up)
- Magnetic position control
- Performance and burn control (and steady-state)
- Start-to-finish discharge simulations

Nucl. Fusion **47** (2007) S385–S403

Principal physics developments evaluated in the ITER design review

Nucl. Fusion **49** (2009) 065012

- Poloidal field requirements
  - The unique combination of high current, high fusion power and long pulse operation in ITER results in very stringent demands on the poloidal field system to provide adequate flux swing, to control the plasma shape, including vertical position, the location of the divertor strike points and the distance to the first wall, in the presence of disturbances.
- Vertical stability
  - To provide reliable operation at the elongation required, a [new] in-vessel coil system has been proposed for increased vertical stability.... Analysis performed to date indicates that this system will satisfy the requirement that values of **Zmax/a of at least 0.05** can be stabilized at acceptable levels of current and voltage and that it can control the plasma vertical position with minimal overshoot.
- ELM control
- RWM control
- Disruption avoidance and mitigation

Nucl. Fusion **49** (2009) 085034 (19pp) doi:10.1088/0029-5515/49/8/085034

Development of ITER 15 MA ELMy H-mode inductive scenario

C.E. Kessel[1], D. Campbell[2], Y. Gribov[2], G. Saibene[3], G. Ambrosino[4], R.V. Budny[1], T. Casper[5], M. Cavinato[3], H. Fujieda[6], R. Hawryluk[1], L.D. Horton[7], A. Kavin[8], R. Kharyrutdinov[9], F. Koechl[10], J. Leuer[11], A. Loarte[2], P.J. Lomas[12], T. Luce[11], V. Lukash[13], M. Mattei[14], I. Nunes[15], V. Parail[12], A. Polevoi[2], A. Portone[3], R. Sartori[3], A.C.C. Sips[7], P.R. Thomas[3], A. Welander[11] and J. Wesley[11]

Abstract

The poloidal field (PF) coil system on ITER, which provides both feedforward and feedback control of plasma position, shape, and current, is a critical element for achieving mission performance. Analysis of PF capabilities has focused on the 15 MA $Q = 10$ scenario with a 300–500 s flattop burn phase. The operating space available for the 15 MA ELMy H-mode plasma discharges in ITER and upgrades to the PF coils or associated systems to establish confidence that ITER mission objectives can be reached have been identified. Time dependent self-consistent free-boundary calculations were performed to examine the impact of plasma variability, discharge programming and plasma disturbances. Based on these calculations a new reference scenario was developed based upon a large bore initial plasma, early divertor transition, low level heating in L-mode and a late H-mode onset. Static equilibrium analyses for this scenario, which determine PF coil currents to produce a given plasma configuration, indicate that the original PF coil limitations do not allow low l_i (<0.8) operation or plasmas with lower flux consumption, and the flattop burn durations were predicted to be less than the desired 400 s. This finding motivates the expansion of the operating space, considering several upgrade options to the PF coils. Analysis was also carried out to examine the feedback current reserve required in the central solenoid and PF coils during a series of disturbances, heating and current drive sources for saving volt-seconds in rampup, a feasibility assessment of the 17 MA scenario was undertaken, and the rampdown phase of the discharge is discussed. Results of the studies show that the new scenario and modified PF system will allow a wide range of 15 MA 300–500 s operation and more limited but finite 17 MA operation.

15 MA ITER Scenario

The discharge is broken into a series of phases and several fiducial points in the discharge are defined, such as start of discharge (SOD), X-point formation (XPF), point in ramp (PIR), start of heating (SOH), start of flattop (SOF), start of burn (SOB), end of burn (EOB) and end of heating (EOH), early rampdown (ERD) and late rampdown (LRD). Shown in figure 2 are the plasma current, plasma internal self-inductance li(3), flux state and βN and βP from a time-dependent simulation of the new scenario described in the previous paragraph, denoting these fiducial points in the discharge by red circles. The primary focus has been on the flattop burn phase bracketed by SOB to EOB and bounded by the blue dashed lines, since it was found to be the most restrictive. In the current rampup and rampdown phases various techniques, such as current ramp rate, density ramp rate and heating, can be used to control the li and flux state, while in the long flattop phase these methods are ineffective.

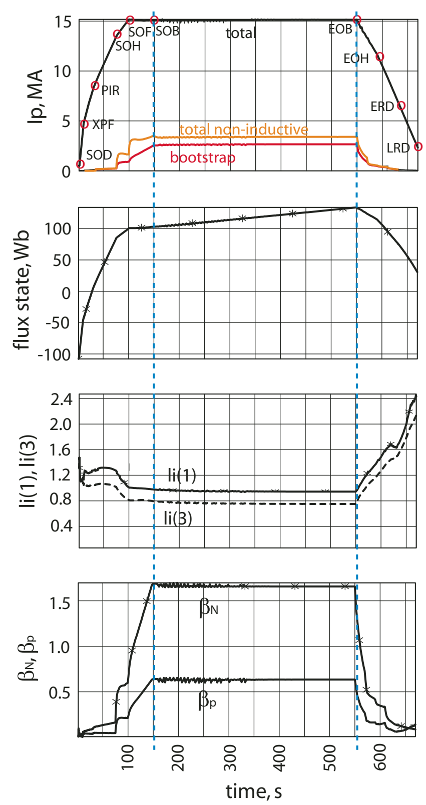

Figure 2. Time histories of the plasma current, flux state, l_i and β_N and β_P utilizing the new rampup strategy. Several fiducial states are identified throughout the discharge. The primary focus of this work is on the flattop phase from SOB to EOB, bounded by the blue dashed lines.

H-Mode creates low-l_i from edge J

Time-dependent calculations with energy transport and bootstrap current were used to provide self-consistent H-mode profile combinations for p(ψ) and j(ψ) for the static equilibrium analysis, which had also been absent from the original analysis.

It is found that the coil current solutions can be affected by the pedestal features, so a range of models is examined to account for the uncertainty in predicting the pedestal in ITER.

Shown in figure 4 are current and pressure profile models used in one of the equilibrium codes (EQ4) to determine the operating space. **The proximity of both the current density and the strong pressure gradient near the plasma edge can affect the PF coil currents required to produce a given plasma boundary.**

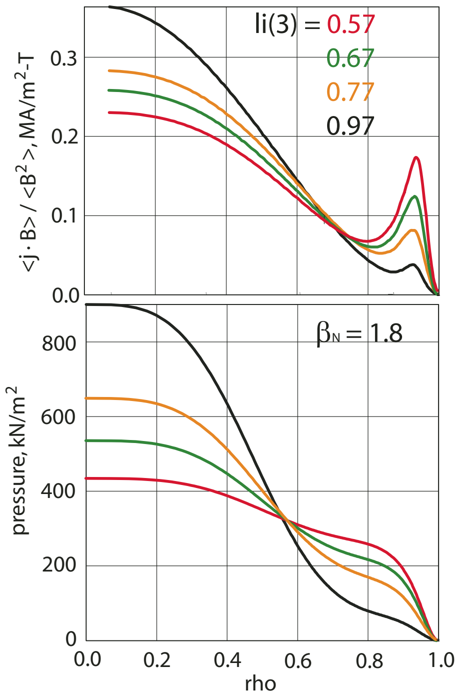

Figure 4. Parallel current density and pressure profiles as a function of the square root of normalized toroidal flux for the EQ4 equilibrium calculations, showing the larger current density and pressure gradient near the plasma edge from the H-mode pedestal as l_i becomes lower.

2007 Design Review Updated PF System for low l_i

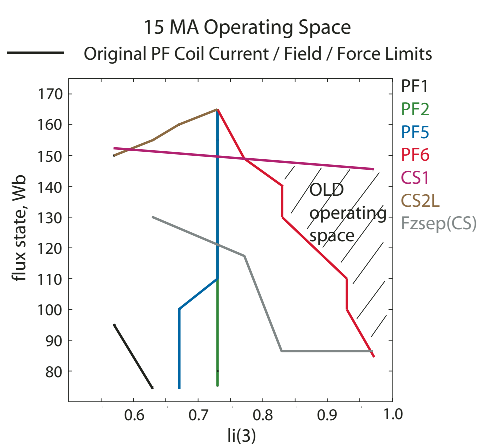

Figure 3. Flux state versus $l_i(3)$ operating space diagram for the original PF coil design parameters. The coloured lines indicate where specific coil current or field limits are exceeded, or where the vertical force limits on the CS stack are exceeded. The operating space that exceeds no coil limits is designated by the hatched region labelled OLD operating space. PF6 and CS1 coils are limiting the operating space available.

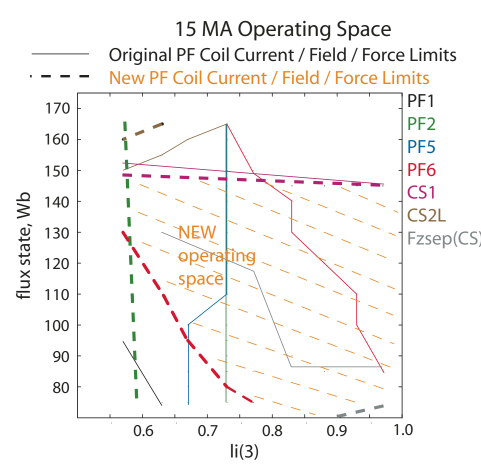

Figure 5. Flux state versus l_i (3) operating space diagram for the new PF coil design parameters and divertor re-design. The coloured lines indicate where specific coil current or field limits are exceeded, or where the vertical force limits on the CS stack are exceeded. The operating space that exceeds no coil limits is designated by the hatched region and labelled NEW operating space. The space is limited by PF6 and PF2 at low l_i, and CS1 at high flux states.

CS Force Limits

Since the CS coils can have currents with opposite signs, the coils experience vertical forces that tend to pull the stack apart, giving rise to the separating force. In addition, the sum of all the vertical forces on the CS coils gives rise to a total force either upwards or downwards, giving rise to a net force. Both of these must be restrained with structures with limited strength, which provides the force limits.

It is found that the feedback systems for the plasma position, shape and current in the simulations are causing the CS3L coil current to remain high and positive during the discharge, which causes a higher separating force. The solution found has been to force the CS3L coil current along a preprogrammed trajectory, removing it from the feedback system.

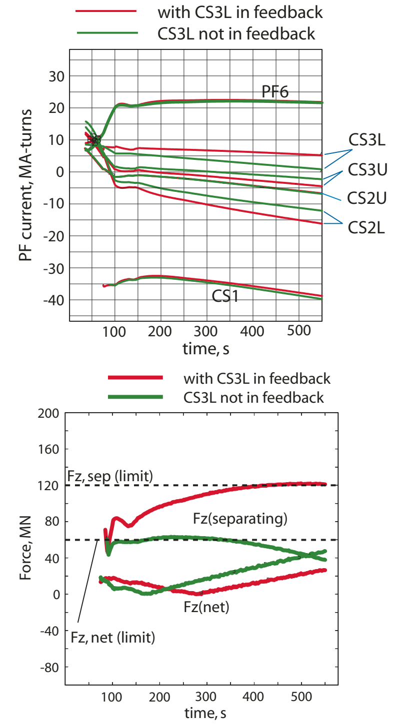

Figure 10. PF coil currents (CS1, CS2, CS3 and PF6) and CS vertical forces versus time during the flattop phase showing their trajectories for a simulation with the CS3L coil participating in the position, shape and current feedback (red) and not participating in the feedback (green). The separating force is reduced significantly by removing CS3L from the feedback, although the net force is increased slightly, but still below its limit. The resulting deviations of the plasma boundary control points were found to be small.

PF “Feedback Reserve”

Several disturbances were identified as providing sufficiently large current requirements on the PF coils that they should be taken into account in determining the operating space for the 15MA reference scenario.

The purpose of determining the current requirements for these disturbances is to subtract this transient current from the maximum PF coil current to establish an operating maximum current on each coil, guaranteeing that the disturbances can be rejected in any part of the discharge

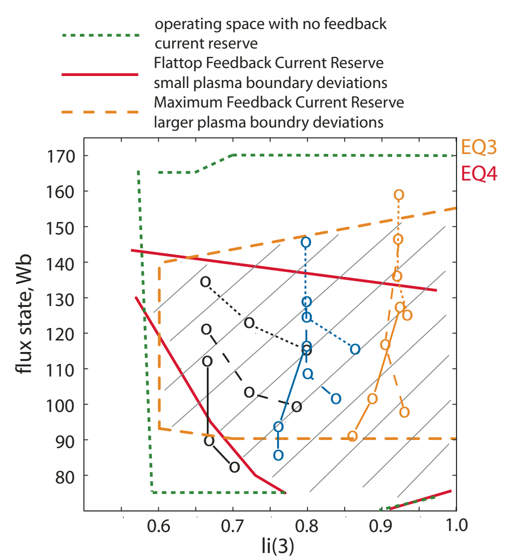

Figure 11. Flux state versus $l_i(3)$ operating space diagram showing the operating space boundaries including feedback current reserve. One equilibrium analysis allows only small plasma boundary deviations and includes the flattop feedback current reserve (red, solid), while the other analysis allows larger plasma boundary deviations and includes the maximum feedback current reserve (orange, dashed). The available operating space is shown by the hatched region. The time-dependent discharge trajectories shown in figure 9 are overlayed on the diagram. The maximum available operating space in the absence of feedback current reserve is shown with the dashed green line for comparison.

Free-Boundary Tokamak Simulation Codes

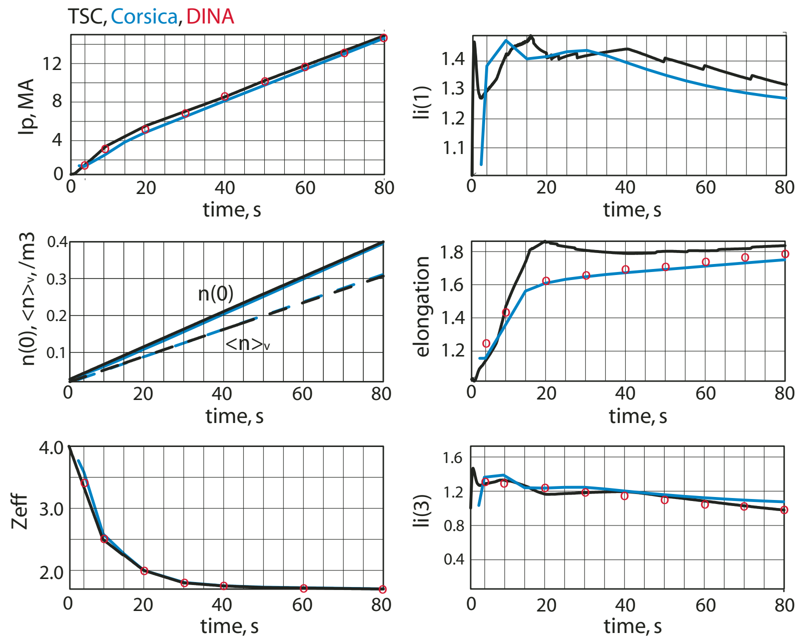

Figure 20. Time histories of the plasma current, density, and Z_{eff} which are prescribed and also $l_i(1)$, elongation, and $l_i(3)$ which are simulated for the ohmic rampup scenario without sawteeth benchmark by TSC (black), Corsica (blue) and DINA (red). The $l_i(3)$ trajectories are reasonably close for all three codes. The elongation was not specified in the benchmark guidelines, and varies due to the different feedback control systems used.

JOURNAL OF COMPUTATIONAL PHYSICS **66**, 481–507 (1986)

Dynamic Modeling of Transport and Positional Control of Tokamaks

S. C. JARDIN, N. POMPHREY, AND J. DELUCIA

Plasma Physics Laboratory, Princeton University, Princeton, New Jersey 08544

Received August 29, 1985; revised December 5, 1985

DEDICATED TO THE MEMORY OF RAYMOND C. GRIMM

We describe a numerical model of a free boundary axisymmetric tokamak plasma and its associated control systems. The plasma is modeled with a hybrid method using two-dimensional velocity and flux functions with surface-averaged MHD equations describing the evolution of the adiabatic invariants. Equations are solved for the external circuits and for the effects of eddy currents in nearby conductors. The method is verified by application to several test problems and used to simulate the formation of a bean-shaped plasma in the PBX experiment.

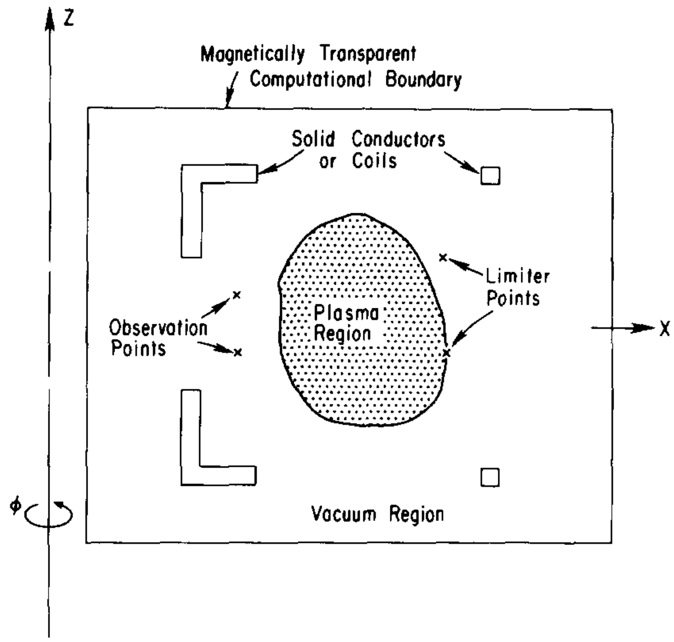

FIG. 1. Computational Domain: Inside a magnetically transparent boundary are a plasma region, a vacuum region, and one or more solid conductor regions. The plasma vacuum interface is in contact with a limiter point. Observation points measure the poloidal flux versus time.

PBX (Princeton Bean eXperiment)

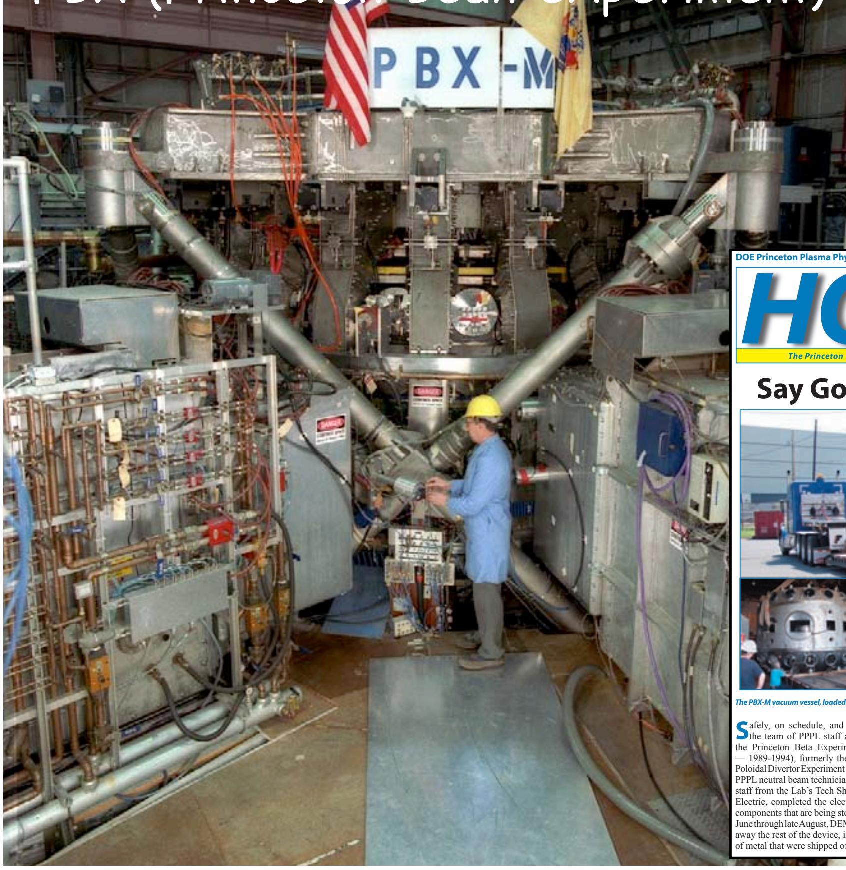

DOE Princeton Plasma Physics Laboratory Vol. 24, No. 11 • August• 2003

HOTLINE

The Princeton Plasma Physics Laboratory is a United States Department of Energy Facility

Say Goodbye to PBX-M Machine

The PBX-M vacuum vessel, loaded onto a flat-bed truck, is taken from the PPPL site. Insert shows workers securing the vessel for its journey.

Safely, on schedule, and within budget. That's how the team of PPPL staff and subcontractors removed the Princeton Beta Experiment-Modification (PBX-M — 1989-1994), formerly the PBX (1985-1989) and the Poloidal Divertor Experiment (PDX — 1978-1985). In June, PPPL neutral beam technicians, machine technicians, and staff from the Lab's Tech Shop, as well as from Powers Electric, completed the electrical safing and removal of components that are being stored for future use. From late June through late August, DEMCO, a subcontractor, cleared away the rest of the device, including more than 352 tons of metal that were shipped off for recycling. Above is the final shipment — the 57,000-pound vacuum vessel — which truckers took from the PPPL site in late August. The former PDX/PBX-M test cell is now cleared to make way for the National Compact Stellarator Experiment (NCSX), which is expected to begin operations in 2007.

Inside ...

PBX (Princeton Bean eXperiment)

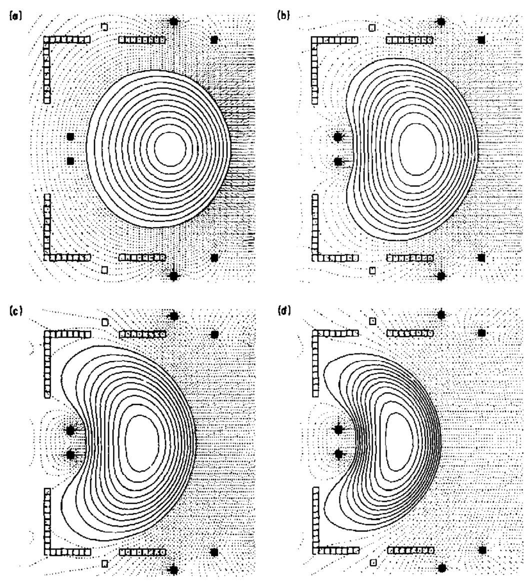

FIG. 10. Snapshots of computed poloidal flux surfaces in PBX experiment at times $t = 0.0$, 150, 200, 300 ms during current ramp-up and shaping phase.

II. EQUATIONS

In an axisymmetric toroidal geometry with symmetry angle ϕ, the magnetic field is expressible in terms of the poloidal flux per radian Ψ and the toroidal field function g in the standard way

$$\mathbf{B} = \nabla\phi \times \nabla\Psi + g\nabla\phi. \tag{1}$$

The function g is a general two-dimensional function whose contours will align themselves with constant poloidal flux contours when the system is in static force balance, i.e., $g = g(\Psi)$ in equilibrium. The toroidal flux Φ within a constant Ψ contour $\Psi = \Psi_c$ is obtained by performing an integral over the contour's interior

$$\Phi \equiv \frac{1}{2\pi} \int_{\Psi < \Psi_c} d\tau\, \mathbf{B} \cdot \nabla\phi = \int_{\Psi < \Psi_c} dx dz\, \frac{g(x, z)}{x}, \tag{2}$$

where (x, ϕ, z) form a cylindrical coordinate system (Fig. 1).

We find it advantageous to express the plasma momentum density $\mathbf{m} = M_i n \mathbf{v}$ in terms of a stream function A, a toroidal component ω, and a potential Ω, thus

$$\mathbf{m} = \nabla\phi \times \nabla A + \omega\nabla\phi + \nabla\Omega. \tag{3}$$

This form for the velocity field allows separate numerical treatment of the incompressible and compressible parts of the flow field. Since the physics governing the wave dynamics of $\nabla \cdot \mathbf{m} = \nabla^2\Omega$ and $\nabla\phi \cdot \nabla \times \mathbf{m} = \nabla \cdot x^{-2}\nabla A$ are determined, respectively, by the longitudinal and transverse characteristics, the time evolution of these to the time that Alfvén waves act to equilibrate force imbalances so that the static equilibrium condition $\mathbf{J} \times \mathbf{B} = \nabla p$ will remain nearly satisfied.

In the absence of Alfvén transit time scale (ideal MHD) instabilities, the inertial terms in the plasma force balance equation are negligible. They are smaller than the magnetic forces by the square of the inverse magnetic Reynolds number, S_{M}^{-2}, where

$$S_{\mathrm{M}}^{-1} = \left(\frac{\eta}{aB_0}\right)\left(\frac{nM_i}{\mu_0}\right)^{1/2} \ll 1. \tag{4}$$

with η the plasma resistivity and a the minor radius. Since the magnitude of the true time-averaged inertial terms are small, we replace them with a more convenient *modified* inertial term which is equivalent to enhancing the plasma mass, dropping the convective derivative term, and choosing a specific form for the plasma viscosity operator,

$$\mathbf{F}_{\mathrm{v}}(\mathbf{m}) = -\nu_1[\nabla^2\mathbf{m} - \nabla(\nabla\cdot\mathbf{m})] - \nu_2\nabla(\nabla\cdot\mathbf{m}). \tag{5}$$

Thus the plasma force balance equation becomes

$$\frac{\partial \mathbf{m}}{\partial t} + \mathbf{F}_{\mathrm{v}}(\mathbf{m}) = \mathbf{J} \times \mathbf{B} - \nabla p. \tag{6}$$

The mass enhancement and viscosity parameters are chosen so that the left-hand side of Eq. (6) remains small enough to be negligible compared to the right-hand side, but not so small as to make forward time integration prohibitive. Further motivation for the modified inertial technique is given in Ref. [9]. It must be verified a posteriori that the modified inertial terms indeed remain small and that the physical results are independent of the fictitious mass and viscosity values over a wide range.

Scalar forms of the momentum equations are obtained by operating on the modified force balance equation, Eq. (6) with $\{\nabla\cdot\}$, $\{\nabla\phi\cdot\nabla\times\}$, and $\{\nabla\phi\cdot\}$. Thus, we obtain

$$\frac{\partial}{\partial t}\nabla^2\Omega + \nabla\cdot\left[\frac{\Delta^*\Psi}{\mu_0 x^2}\nabla\Psi + \frac{g}{\mu_0 x^2}\nabla g + \nabla p - \nu_2\nabla(\nabla^2\Omega)\right] = 0, \tag{6a}$$

$$\frac{\partial}{\partial t}\Delta^* A + x^2\nabla\cdot\left[\frac{\Delta^*\Psi}{\mu_0 x^2}\nabla\Psi\times\nabla\phi + \frac{g}{\mu_0 x^2}\nabla g\times\nabla\phi - \frac{\nu_1}{x^2}\nabla(\Delta^* A)\right] = 0, \tag{6b}$$

$$\frac{\partial}{\partial t}\omega + \mu_0^{-1}\nabla\phi\times\nabla g\cdot\nabla\Psi - \nu_1\Delta^*\omega = 0, \tag{6c}$$

where $\Delta^* \equiv x^2\nabla\cdot x^{-2}\nabla$ is the standard toroidal elliptic operator.

We note here that static solutions to Eqs. (6a)–(6c) with (Ω, A, ω) and their time derivatives set to zero are exact solutions to the full Grad–Shafranov equilibrium equation, i.e.,

$$\Delta^*\Psi + \mu_0 x^2 \frac{d}{d\Psi} p(\Psi) + \frac{1}{2}\frac{d}{d\Psi} g^2(\Psi) = 0. \tag{7}$$

Transient solutions for Ψ, p, and g are always within $\varepsilon \equiv S_M^{-2}$ of satisfying Eq. (7).
Faraday's Law, and an Ohm's law of the form

$$\mathbf{E} + \mathbf{v}\times\mathbf{B} = \mathbf{R}, \tag{8}$$

where $\mathbf{R}$ contains the nonideal terms, yield evolution equations for the poloidal flux and toroidal field functions

$$\frac{\partial}{\partial t}\Psi + \frac{1}{\rho_0}(\nabla\phi\times\nabla A\cdot\nabla\Psi + \nabla\Omega\cdot\nabla\Psi) = x^2\nabla\phi\cdot\mathbf{R}, \tag{9}$$

$$\frac{\partial}{\partial t}g + x^2\nabla\cdot\left[\frac{g}{\rho_0 x^2}(\nabla\phi\times\nabla A + \nabla\Omega) - \frac{\omega}{\rho_0 x^2}\nabla\phi\times\nabla\Psi - \nabla\phi\times\mathbf{R}\right] = 0. \tag{10}$$

Here, $\rho_0 \equiv n_0 M_i$ is a constant, having the role of the enhanced mass density.

Since the toroidal magnetic field is due primarily to external currents, it is relatively immobile, making it convenient to evolve the surface-averaged thermodynamic variables relative to magnetic coordinate surfaces containing a fixed amount of toroidal flux. To derive the surface-averaged evolution equations, we decompose the cross-field fluid velocity into two parts

$$\mathbf{v}\cdot\nabla\Psi=\mathbf{v}_{\mathrm{c}}\cdot\nabla\Psi+\mathbf{v}_{\mathrm{R}}\cdot\nabla\Psi, \tag{11}$$

where $\mathbf{v}_{\mathrm{c}}\cdot\nabla\Psi$ is associated with the evolution of the coordinate surfaces, and $\mathbf{v}_R\cdot\nabla\Psi$ is the fluid flow relative to these surfaces. For magnetic coordinate surfaces evolving with fixed toroidal flux Φ, we have from Eq. (10),

$$\mathbf{v}_{\mathrm{R}}\cdot\nabla\Psi=\frac{x^2}{g}\nabla\phi\times\mathbf{R}\cdot\nabla\Psi \tag{12}$$

and

$$\frac{\partial}{\partial t}\left(\frac{1}{q}\oint\frac{dl}{B_{\mathrm{p}}}\right)=\frac{\partial}{\partial\Psi}\left(\frac{1}{q}\oint\frac{dl}{B_{\mathrm{p}}}\mathbf{v}_{\mathrm{c}}\cdot\nabla\Psi\right). \tag{13}$$

Here, $q\equiv(2\pi)^{-1}\,\partial\Phi/\partial\Psi$ is the safety factor, $B_{\mathrm{p}}\equiv|\nabla\phi\times\nabla\Psi|$ is the magnitude of the poloidal magnetic field, and the line integrals are around a contour in a poloidal cross section at $\Psi=$ const. Using Eqs. (11)–(13) to eliminate the velocity from the

Here, $q\equiv(2\pi)^{-1}\,\partial\Phi/\partial\Psi$ is the safety factor, $B_{\mathrm{p}}\equiv|\nabla\phi\times\nabla\Psi|$ is the magnitude of the poloidal magnetic field, and the line integrals are around a contour in a poloidal cross section at $\Psi=$ const. Using Eqs. (11)–(13) to eliminate the velocity from the mass and energy conservation equations, we obtain [10] one-dimensional evolution equations for the differential number density $N'\equiv n\,\partial V/\partial\Phi$, and the differential total and electron entropy densitities $\sigma\equiv p(\partial V/\partial\Phi)^{5/3}$ and $\sigma_{\mathrm{e}}\equiv p_{\mathrm{e}}(\partial V/\partial\Phi)^{5/3}$, with respect to magnetic surfaces containing a fixed toroidal flux.

$$\frac{\partial}{\partial t}N'=-\frac{\partial}{\partial\Phi}(N'\Gamma)+S_{\mathrm{N}}, \tag{14}$$

$$\frac{\partial}{\partial t}\sigma=\frac{2}{3}\left(\frac{\partial V}{\partial\Phi}\right)^{2/3}\left[V_L\frac{\partial K}{\partial\Phi}-\frac{\partial}{\partial\Phi}(Q_i+Q_{\mathrm{e}})+\frac{\partial V}{\partial\Phi}(S_{\mathrm{e}}+S_i)\right], \tag{15}$$

$$\frac{\partial}{\partial t}\sigma_{\mathrm{e}}=\frac{2}{3}\left(\frac{\partial V}{\partial\Phi}\right)^{2/3}\left[V_L\frac{\partial K}{\partial\Phi}-\frac{\partial Q_e}{\partial\Phi}+\frac{\partial V}{\partial\Phi}\left(-\Gamma\frac{\partial p_i}{\partial\Phi}+Q_{\Delta\mathrm{e}}+S_{\mathrm{e}}\right)\right]. \tag{16}$$

Time derivatives are with respect to surfaces containing fixed toroidal flux Φ. We have defined the differential volume

$$\frac{\partial V}{\partial\Phi}=\frac{\partial}{\partial\Phi}\oint d\tau=\frac{1}{q}\oint\frac{dl}{B_{\mathrm{p}}}, \tag{17}$$

the loop voltage

$$V_L=\frac{2\pi\langle\mathbf{R}\cdot\mathbf{B}\rangle}{\langle\mathbf{B}\cdot\nabla\phi\rangle}, \tag{18}$$

and the total toroidal current within a flux surface

$$K=\oint\mathbf{B}_{\mathrm{p}}\cdot\mathbf{d}l=\oint\frac{dl|\nabla\Psi|}{x}. \tag{19}$$

The particle flux and electron and ion heat fluxes are defined as

$$\Gamma=2\pi q[\langle x^2\mathbf{R}\cdot\nabla\phi\rangle-\langle\mathbf{R}\cdot\mathbf{B}\rangle/\langle B\cdot\nabla\phi\rangle], \tag{20}$$

$$Q_i=\frac{\partial V}{\partial\Phi}\left[\langle\mathbf{q}_i\cdot\nabla\Phi\rangle+\frac{5}{2}p_i\Gamma\right], \tag{21}$$

$$Q_e=\frac{\partial V}{\partial\Phi}\left[\langle\mathbf{q}_{\mathrm{e}}\cdot\nabla\Phi\rangle+\frac{5}{2}p_{\mathrm{e}}\Gamma\right], \tag{22}$$

where $\mathbf{q}_i$ and $\mathbf{q}_e$ are the random heat flux vectors. We have introduced the flux surface average operator in Eqs. (18), (20), (21), (22),

$$\langle a\rangle\equiv\frac{\oint(dl/B_{\mathrm{p}})\,a}{\oint(dl/B_{\mathrm{p}})}.$$

B. *Vacuum Region*

The vacuum region is defined by either having $\Psi > \Psi_L$, where Ψ_L is the first plasma flux surface in contact with a limiter or by being separated from the plasma by a magnetic x point. We treat the vacuum region as a low temperature, zero pressure gradient plasma in which currents can appear. In the limit as the vacuum conductivity approaches zero, the magnitude of these currents will go to zero and the magnitude of the magnetic diffusion coefficient will approach infinity. Thus, Eq. (6) (with $\nabla p = 0$), and Eqs. (9) and (10) are solved in the vacuum region, with a classical resistivity, Eq. (26), based on a constant electron temperature $T_e = T_V$. The vacuum temperature, normally a few eV, is much less than the central plasma temperature, normally 0.1 to 3.0 keV; however, it is not zero. This vacuum temperature and a vacuum density, n_v, serve as boundary conditions on the surface-averaged plasma evolution Eqs. (14) through (16). Since the plasma temperatures and densities will approach these values smoothly, all physical quantities are smooth and continuous across the plasma-vacuum interface, and no special boundary treatment is required there. Again, we must verify a posteriori that the physical results converge to a value independent of the vacuum temperature T_v.

At the outer boundary of the vacuum region, i.e., the computational domain boundary, we model an insulating, magnetically transparent boundary by prescribing that the toroidal field strength g and the poloidal flux Ψ be consistent with the instantaneous plasma and coil currents. Thus, on the boundary points $\mathbf{x}_b$,

$$g(\mathbf{x}_b) = g_0 = \frac{\mu_0 I_{TF}}{2\pi}, \tag{32}$$

$$\Psi(\mathbf{x}_b, t) = \frac{\mu_0}{2\pi} \int_p G(\mathbf{x}_b, \mathbf{x})\, J_\phi(\mathbf{x}, t)\, d^2\mathbf{x} + \sum_{i=1}^{N} \frac{\mu_0}{2\pi} G(\mathbf{x}_b, \mathbf{x}_i)\, I_i. \tag{33}$$

Here, I_{TF} is the total current in all the toroidal field coils, $G(\mathbf{x}_b, \mathbf{x})$ is the analytic exterior Green's function for an axisymmetric current filament [11],

C. *Solid Conductors*

The physical material velocity is zero in the solid conductors. Allowing for the possibility of an external circuit connection supplying an applied voltage $V(t)$, the poloidal flux evolution equation, the analogue of Eq. (9) in the plasma, becomes

$$\frac{\partial}{\partial t} \Psi = \mu_0^{-1} \eta \Delta^* \Psi + (2\pi)^{-1} V(t). \tag{45}$$

We note here a direct analogy between the poloidal flux evolution equation in the conductor, Eq. (45), and a discrete circuit equation. Suppose a single isolated mesh

To model the control systems in the tokamak, we allow the applied voltage $V(t)$ appearing in Eqs. (45) and (51) to be a function of the instantaneous poloidal flux values at two or more observation points $\mathbf{x}^{\mathrm{OBS}}$, and of other global parameters. A useful form for most applications is to specify the positions of two observation points $\mathbf{x}_1^{\mathrm{OBS}}$ and $\mathbf{x}_2^{\mathrm{OBS}}$, a linear gain α and a normalized flux offset β so that

$$V(t) = \alpha \left[\Psi(\mathbf{x}_1^{\mathrm{OBS}}) - \Psi(\mathbf{x}_2^{\mathrm{OBS}}) - \frac{\beta I_p(t)}{I_{p0}} \right], \tag{52}$$

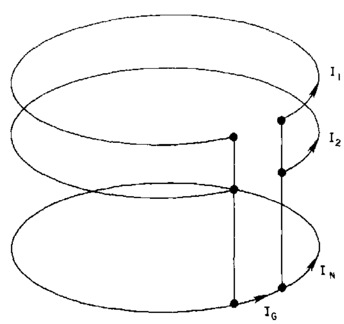

FIG. 2. Generalized poloidal field circuit configuration allows for a gap with gap current I_G and gap resistivity r_G.

where $I_p(t)$ and I_{p0} are instantaneous and reference values of the total plasma current.

It is necessary to generalize the circuit Eq. (45) to model conductors with toroidal cuts or toroidally localized high resistance regions such as bellows or vacuum vessels with toroidal breaks. We take a group of N poloidal field conductors to be connected as in Fig. 2 with a small common gap with gap resistance r_G and gap current

$$I_G = \sum_{n=1}^{N} I_n = \Delta A \sum_{n=1}^{N} \mu_0^{-1} \Delta^* \Psi_n / x_n. \tag{53}$$

The generalization to Eq. (45) is then simply, for $n = 1, N$,

$$\frac{\partial}{\partial t} \Psi_n = \mu_0^{-1} \eta_n \Delta^* \Psi_n + (2\pi)^{-1} [V_n(t) + r_G I_G]. \tag{54}$$

We verify that Eqs. (53) and (54) have the correct limits, reducing to Eq. (45) when $r_G \to 0$ and forcing $I_G = 0$ when $r_G \to \infty$.

Finally, we consider the boundary conditions on the velocity variables A and Ω at the interface between the conductors and the vacuum region. For the same considerations as discussed in Section IIB the appropriate boundary conditions are given by Eq. (39). However, imposing internal boundary conditions and thus making the computational region multiply connected would rule out the use of fast

C. *Resistive Axisymmetric Stability Test*

A model problem consisting of an elliptical cross-sectional plasma and top–bottom finite resistivity plates is set up as shown in Fig. 6. At $t = 0$, the plasma is given a perturbation by applying a radial magnetic field to induce asymmetry in the vertical direction. The conducting plates stabilize the plasma on the ideal MHD, Alfvén wave transit time scale, but an instability persists on the much slower time

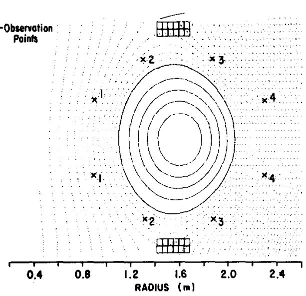

FIG. 6. Elliptical plasma is stabilized on fast (ideal) time scale by conducting plates. Observation points record flux difference of instability caused by finite resistivity of conductors.

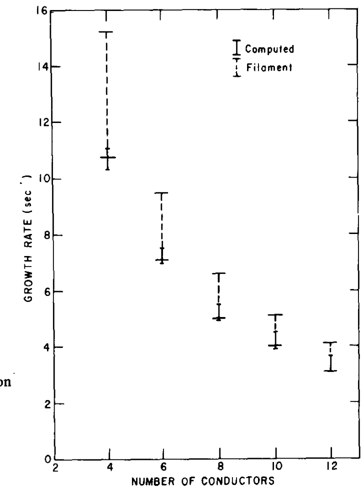

FIG. 7. Growth rates versus conductor size for elliptical plasma instability of Fig. 6. Also shown are predictions of a wire filament model located within $\pm 4\%$ of the minor radius about the current centroid.

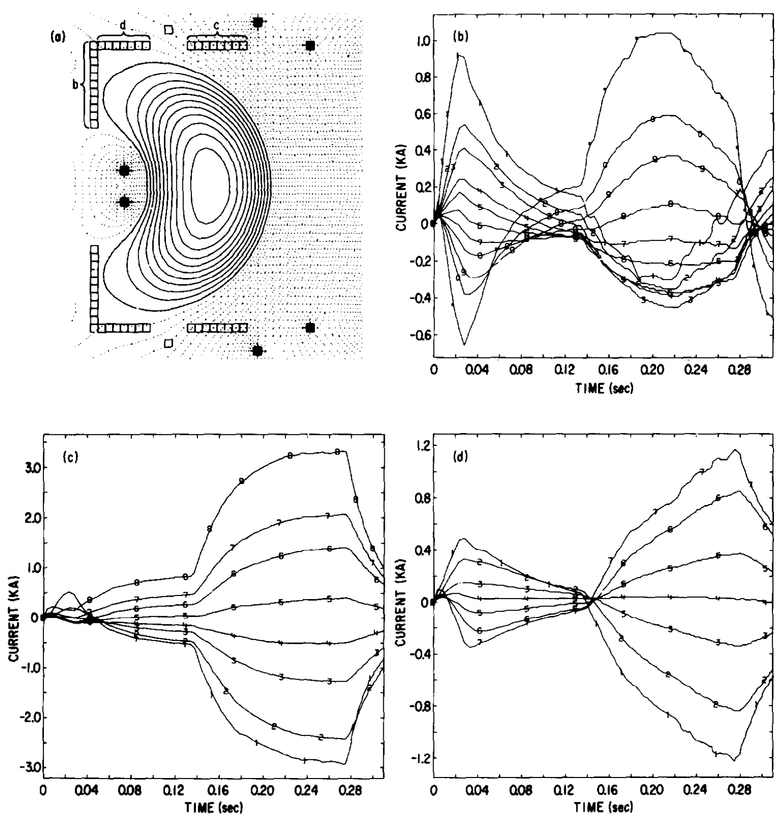

FIG. 12. Time history of current distribution in passive conducting plate segments for PBX calculation of Fig. 10.

We illustrate in Fig. 10 the poloidal magnetic flux surfaces at several times during the simulation. The profiles of the toroidal current and pressure across the plasma midplane are shown in Fig. 11. It is seen that the current peaks on the outside of the discharge during the current ramp-up phase but eventually penetrates into the plasma. In Fig. 12 we plot the distribution of induced axisymmetric eddy currents in the three sections of passive conducting plates in the upper half of PBX. The presence of a gap in each of the plates constrains the net current in each of the plates to be zero.

One measure of the accuracy of the simulation is the ratio of the kinetic energy to the magnetic energy in the computational domain. This quantity remained smaller than 5×10^{-6} during the entire calculation, verifying that the inertial terms in the force balance Eq. (6) are indeed always small. This implies that the plasma evolves through a series of near-equilibrium states.

VI. Summary

We have described a new method for computing the free boundary time evolution of an axisymmetric toroidal plasma evolving due to plasma transport and resistive dissipation, external heating, and changing currents in the poloidal field coils. The method is based on introducing several artificial parameters into the zero inertia MHD and vacuum equations, and by taking the limit as these parameters become small. Code verification examples were presented as well as an application demonstrating the formation and positional stability of a bean-shaped plasma in the PBX device.

Summary

- Tokamak operations and control will be key to the success of ITER

- MHD/computational tools, like TSC, can make detailed engineering and control simulations that design and give confidence to ITER operations

- Discharge planning with simulations is essential to the effective use of ITER